Title
Determination of Ground Subsidence Around Snow Fences in the Arctic Region

Journal
Lithosphere, 2025(1)

ISSN
1941-8264

Authors
Kim, Kwansoo
Ju, Hyeontae
Chi, Junhwa
et al.

Publication Date
2025-01-30

DOI
10.2113/2025/lithosphere_2024_215

GeoScienceWorld
Lithosphere
Volume 2025, Number 1, Article ID lithosphere_2024_215, 13 pages
https://doi.org/10.2113/2025/lithosphere_2024_215

Lithosphere

Research Article

Determination of Ground Subsidence Around Snow Fences in the Arctic Region

Kwansoo Kim,[1] Hyeontae Ju,[1,2] Junhwa Chi,[3] Ji Young Jung,[4] Sungjin Nam,[4] Sang-Jong Park,[5] Baptiste Dafflon,[6] Joohan Lee,[1] and Won-Ki Kim[7]

[1]*Center of Technology Development, Korea Polar Research Institute, Incheon, 21990, South Korea*
[2]*Department of Energy Resource Engineering, Inha University, Incheon, 22212, South Korea*
[3]*Major of Big Data Convergence, Division of Data Information Sciences, Pukyong National University, Busan, 48513, South Korea*
[4]*Division of Life Sciences, Korea Polar Research Institute, Incheon, 21990, South Korea*
[5]*Division of Ocean and Atmosphere Sciences, Korea Polar Research Institute, Incheon, 21990, South Korea*
[6]*Climate & Ecosystem Sciences Division, Lawrence Berkeley National Laboratory, Berkeley, California, 94720, USA*
[7]*Department of Earth and Environmental Sciences, Chungbuk National University, Cheongju, 28644, South Korea*

Correspondence should be addressed to Won-Ki Kim; konekee@chungbuk.ac.kr and Joohan Lee; joohan@kopri.re.kr

Received 13 September 2024; Accepted 31 December 2024; Published 30 January 2025

Academic Editor: Yongchae Cho

In this study, we analyzed the effects of snow cover changes caused by snow fences (SFs) installed in 2017 in the Alaskan tundra to examine ground subsidence. Digital surface model data obtained through LiDAR-based remote sensing in 2019 and 2022, combined with a field survey in 2021, revealed approximately 0.2 m of ground subsidence around the SF. To investigate the relationship between SF-induced snow cover changes and ground subsidence, geophysical methods, electrical resistivity tomography (ERT) and ground-penetrating radar (GPR), were applied in 2023 to analyze subsurface characteristics. The increased snow cover due to the SF-enhanced insulation, delaying the penetration of winter cold into the subsurface. This delay caused subsurface temperatures to decrease more slowly, melting the upper permafrost and increasing the thickness of the active layer. ERT and GPR surveys well delineated the boundary between the active layer and permafrost, confirming that the increased snow cover thickened the active layer. This thickening led to the melting of pore ice, causing water runoff and ground compaction, which resulted in subsidence. The runoff also formed channels flowing eastward over the SF. This study highlights how changes in snow cover can influence active layer properties, leading to localized environmental changes and ground subsidence.

1. INTRODUCTION

In recent years, global warming has triggered numerous environmental changes in the polar regions. For instance, increasing average temperatures have caused polar glaciers to melt and sea levels to rise. As atmospheric temperatures rise and the ground absorbs more solar energy, the active layer and permafrost undergo changes. The snow accumulated during winter melts rapidly and infiltrates the surface, allowing heat-laden water to melt the upper layers of permafrost and thicken the active layer. This process leads to subsidence and the tilting of buildings in many inhabited areas of the polar region. These ongoing changes in the active layer and permafrost conditions in the polar region are expected to continue and intensify.

As the amount of winter snowfall increases, the condition of the soil is also impacted. Snow accumulation delays the onset of freezing soil temperatures and raises average soil temperatures. These changes can significantly alter plant growth conditions and the active layer [1]. The rise in atmospheric temperatures has led to precipitation occurring at times typically expected for winter snowfall or to more intense snowfall when temperatures are below freezing. This phenomenon is believed to result from

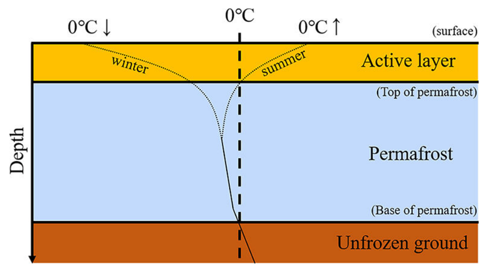

FIGURE 1: Schematic temperature profiles of the active layer, permafrost, and unfrozen ground (reproduced from Kim et al. [57]).

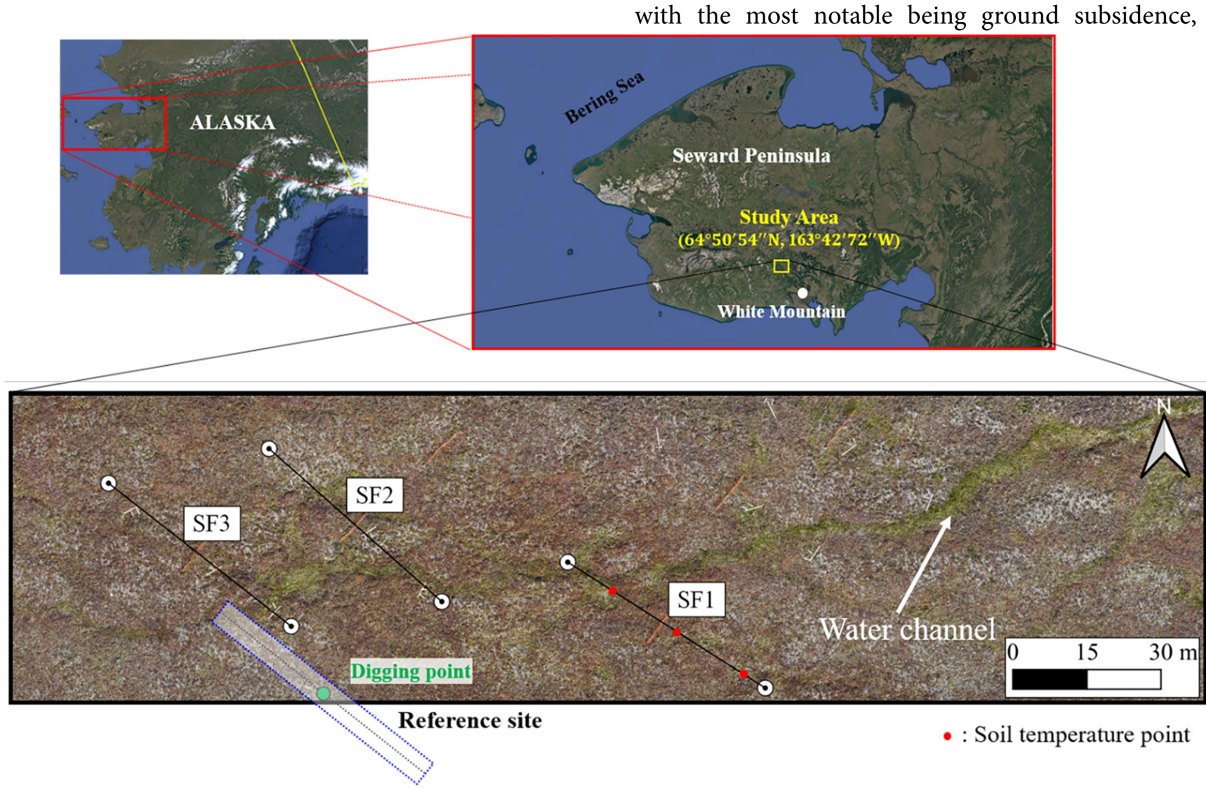

FIGURE 2: Location map of the study area and aerial photograph of snow fence installation.

previously fallen rainfall or significant moisture content in the atmosphere transported from the ocean [2].

Several researchers have used various structures in the Arctic region to investigate changes in surface vegetation and the active layers in response to variations in air temperature and snow cover [3–5]. Changes in snow cover induce environmental alterations, making them a subject of active research. A common method for investigating snow cover change involves artificially altering snow cover by installing snow fences (SFs) and analyzing their effects [6]. SFs are used to manage snow accumulation on highways in the snowy Alaskan region of the United States during winter or to mitigate avalanche damage on steep slopes at high altitudes in the Alps during winter [7]. SFs are typically installed for human convenience; however, in recent years, they have been increasingly used in climate change research to artificially modify snow cover and study topographic and ecosystem changes in response to snowfall [8–10]. Nevertheless, additional appropriate methods are needed to gain deeper insights into the impact of snow cover changes on the subsurface.

The objective of this study was to artificially alter snow cover in polar regions by installing SFs to gain insight into the effects of environmental change on snow cover in these regions. Since 2017, SFs have been installed in early September and removed at the end of June in the following year. However, from 2020 to 2022, due to the global pandemic, the SFs remained in place without removal, and only partial environmental data were collected. During this period, the effects of changing snow cover accumulated, with the most notable being ground subsidence, which became visible across the study area, with significant subsidence observable to the naked eye. This subsidence is likely associated with changes in the active layer, a common feature of permafrost regions such as the polar regions. Various geophysical surveys were conducted for this study. To quantitatively observe changes in topography, remote sensing (LiDAR) using drones was performed. Additionally, electrical resistivity tomography (ERT) and ground-penetrating radar (GPR) were used to identify changes in subsurface characteristics. From the ERT and GPR surveys, changes in the lower interface of the active layer can be effectively identified.

The earliest LiDAR systems, developed in the 1930s, used light, but by 1960, scientists had advanced to using laser pulses to measure the travel time between the sensor and the target [11]. The LiDAR technique has continually evolved and remains widely used in optical research.

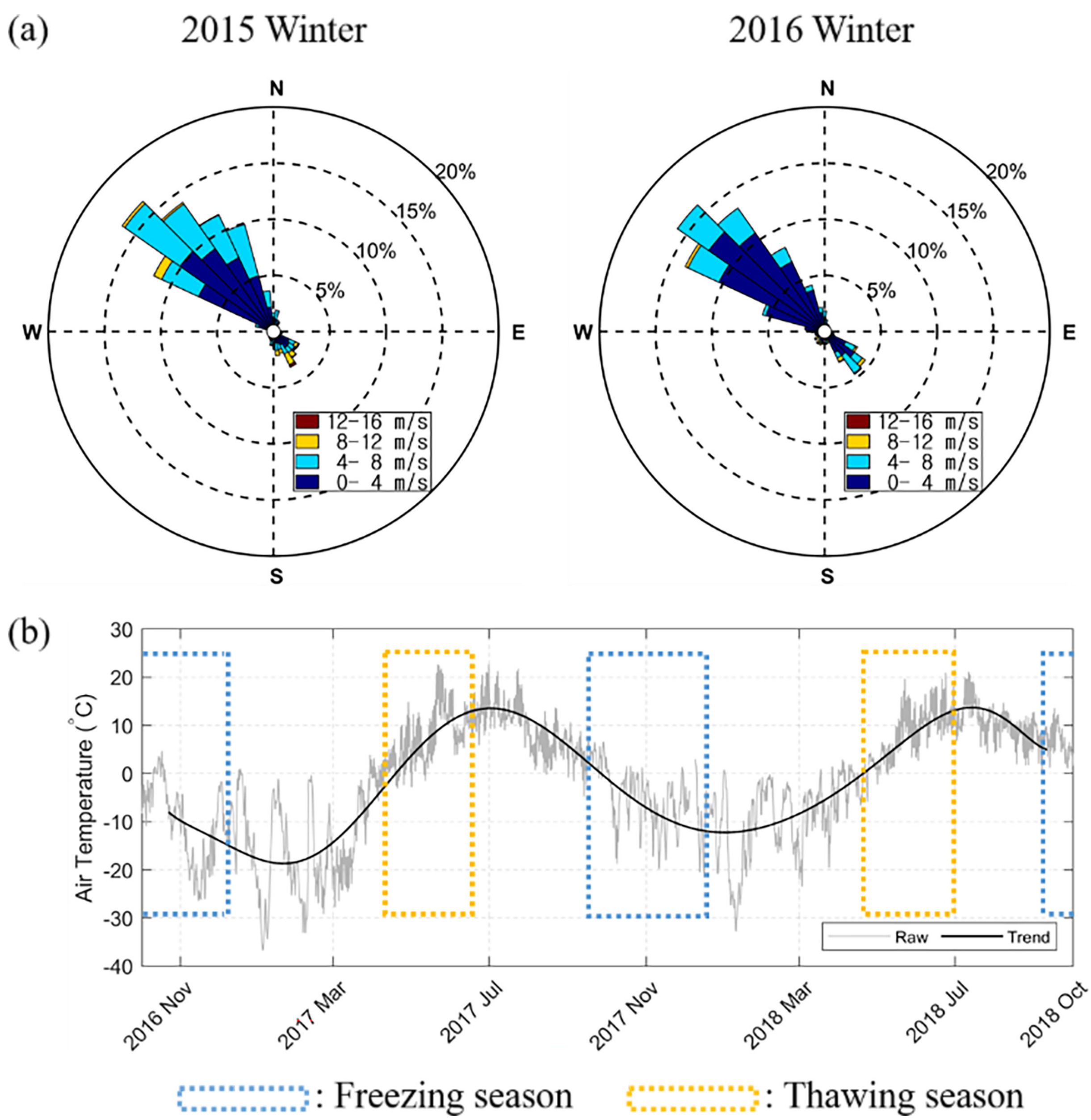

Figure 3: (a) Wind rose diagrams for the winters of 2015 and 2016 and (b) temperature observations for October 2016 through October 2018.

Additionally, LiDAR technology has progressively improved and is now actively employed in various applications. In the late 1990s, LiDAR began to be used for spatial information applications, such as geographical information systems [12]. With technological advancements, the applicability of these systems has improved due to enhanced hardware performance and data processing techniques, leading to their integration with inertial measurement units (IMUs) and the global positioning system [13, 14]. More recently, LiDAR has been integrated into unmanned aerial vehicles (UAVs), such as aerial drones, to enhance surveying efficiency [15].

An electrical resistivity survey is used to obtain subsurface information by detecting variations in the electrical properties of the subsurface medium. This technique has been recently applied in various fields, such as reservoir leak detection, tunnel construction, landfill monitoring, groundwater analysis, subsurface cavity investigations, and glacier and fault zone identification [16–21]. The electrical resistivity values of water and ice differ significantly in their natural states. Water is highly conductive, whereas ice is a poor conductor with high electrical resistivity. By leveraging these properties, electrical resistivity surveys have been conducted in polar regions to identify boundary changes between the active layer and permafrost [22–25]. Recently, the thawing of frozen regions due to climate change has caused

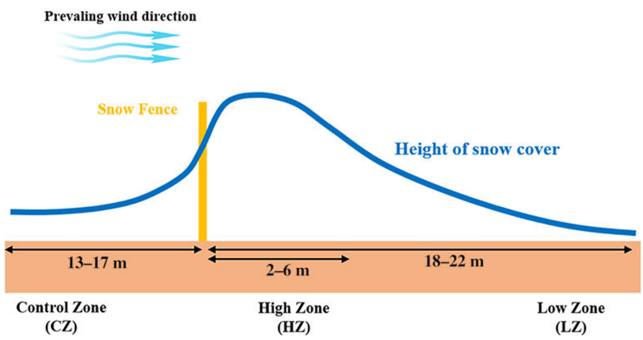

FIGURE 4: Schematic of the snow fence installation with snow cover.

whereas Chapter 3 outlines the environmental characteristics of the study area and the SFs. In Chapter 4, environmental changes in the natural geology after the installation of the SFs are analyzed using geophysical methods such as remote sensing (LiDAR), ERT, and GPR. Finally, the concluding chapter provides a summary and scientific insights based on the analysis.

2. PERMAFROST AND THE ACTIVE LAYER

Permafrost refers to ground that remains frozen at temperatures below 0.0°C for more than 2 years and is predominantly found in high latitudes and alpine regions. Approximately 23.9% of the land in the northern hemisphere is permafrost [42]. The classification of permafrost is based on the percentage of ground that is frozen: continuous permafrost is characterized by more than 90% of frozen ground, whereas discontinuous permafrost is when 50%–90% of the ground is frozen. Additionally, sporadic permafrost is classified as having 10%–50% frozen ground, and isolated permafrost is defined as having less than 10% frozen ground [43].

The active layer refers to the layer of soil that thaws during the summer and refreezes in the late autumn in an environment containing permafrost, repeating this process annually [44, 45]. Figure 1 shows the relationship between the permafrost and the active layer with respect to temperature variation. Recently, global warming has increased the average global temperature, resulting in longer summers and shorter winters. Additionally, current winter atmospheric temperatures are higher than in previous years, causing the active layer to thaw earlier and refreeze later. This shift changes the period during which the active layer remains frozen. Alongside rising atmospheric temperatures, other factors contribute to the development of active layers in frozen regions, including frequent winter rainfall, soil warming, water infiltration from melting snow, and surface runoff.

Changes in the water content of these layers affect the heat transfer properties of the subsurface in the region. As suggested by Fatouki in 1981 [46], the bulk thermal conductivity of the active layer can be estimated from the soil thermal conductivity under both dry and wet conditions, assuming that the composition of air, water, and

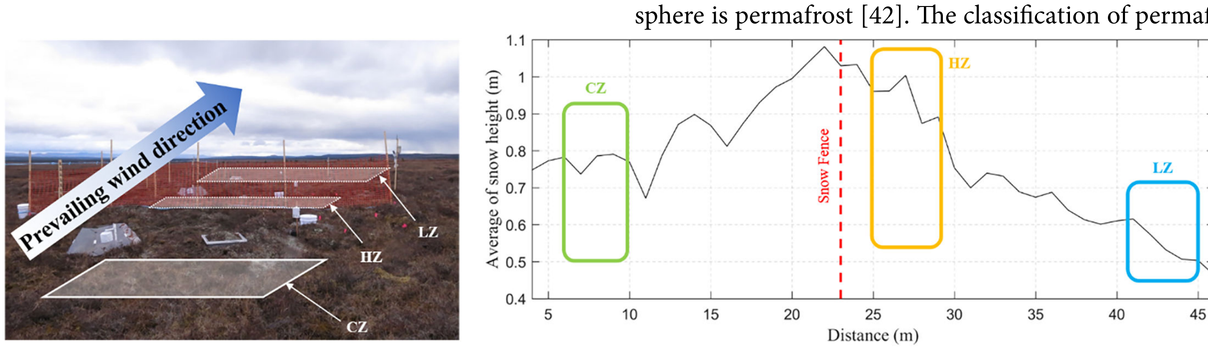

(a) (b)

FIGURE 5: (a) A photograph of the in situ installation and (b) the average snow cover for the three snow fences observed in February 2021.

engineering challenges and slope instability when constructing infrastructure such as roads, railways, pipelines, and power grids. Consequently, the use of electrical resistivity surveys in these environments has increased.

GPR surveys, which utilize changes in the electromagnetic (EM) properties of the subsurface, involve transmitting high-frequency EM waves into the ground and analyzing the reflected signals. Due to their high resolution and versatility, GPR surveys have been applied for various purposes, including sediment stratigraphy, underground cavity detection, unexploded ordnance detection, locating buried pipes, identifying rebar in concrete, excavating historical sites and artifacts, and detecting hidden objects such as corpses or gold bullion [26]. Notably, GPR surveys are extensively used in polar regions to measure glacier thickness and crevasses, detect and size ice lakes, investigate sublake taliks in frozen areas, and assess thickness variations in the active layers [27–33]. An additional benefit of GPR surveys is that they can be conducted with fewer personnel than other geophysical survey methods.

In addition to ERT and GPR, other physical survey methods are widely used for permafrost research. EM methods are used to identify permafrost because of their ease of use [34–36]. Elastic wave refraction method exploration is actively used because the boundary between the active layer and the permafrost layer can be clearly distinguished due to the velocity difference between the two layers [37–41].

The remainder of this article is structured as follows: Chapter 2 introduces permafrost and the active layer,

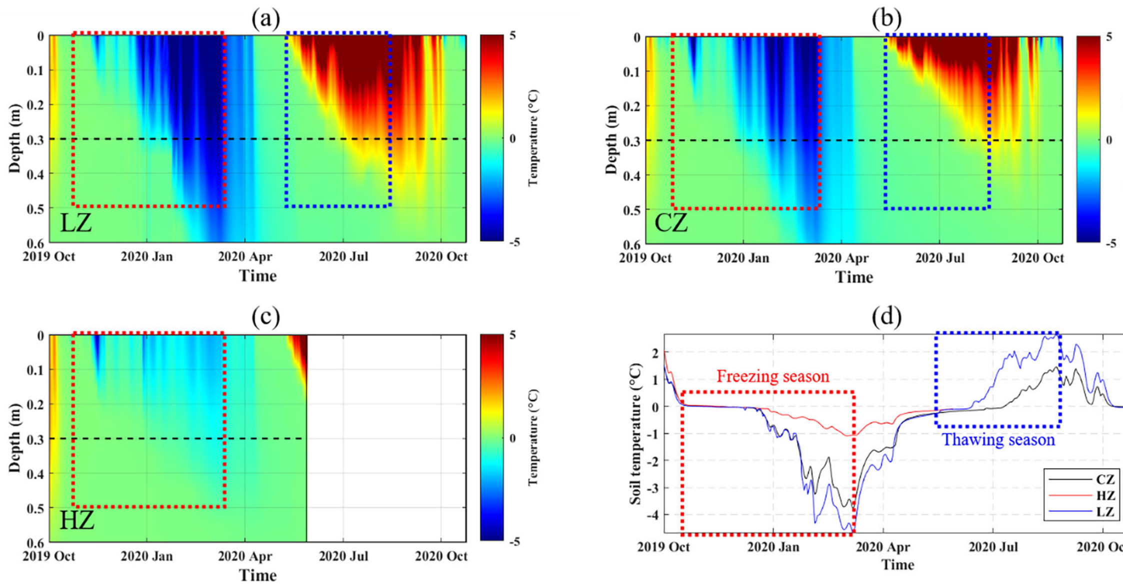

FIGURE 6: (a)–(c) Ground temperatures as a function of depth by date, and (d) comparison of ground temperatures at a depth of 0.3 m over time: (a) LZ, (b) CZ, (c) HZ. The red and blue dotted boxes represent the freezing and thawing seasons, respectively.

TABLE 1: The major specification of LiDAR sensor.

Number of channels	16
Maximum measurement range	100 m
Range accuracy (typical)	Up to ±3 cm
Field of view	−10°–10° (vertical); 360° (horizontal)
Angular resolution	1.33° (vertical); 0.1°–0.4° (horizontal)
Rotation rate	5–20 Hz
Laser wavelength	903 nm
Laser pulses per second	300,000 (single return mode) 600,000 (dual return mode)

organic content within the pores of the soil layer is known. For instance, comparing the thermal conductivity of clay and sand with 40% porosity in dry and wet environments reveals that dry clay has a thermal conductivity of about 0.25 $W \cdot m^{-1}K^{-1}$, which is approximately one-sixth that of saturated clay at 1.6 $W \cdot m^{-1}K^{-1}$. Similarly, dry sand has a thermal conductivity of about 0.3 $W \cdot m^{-1}K^{-1}$, which is approximately one-seventh that of saturated sand at 2.2 $W \cdot m^{-1}K^{-1}$. This indicates that both materials exhibit higher thermal conductivity when saturated than when dry, implying that the active layer, which contains abundant meltwater, also has higher thermal conductivity.

The infiltration of snowmelt water, which contains heat energy, into the ground during accelerated thawing periods increases soil temperature, which subsequently transfers heat energy to the upper part of the permafrost beneath the active layer, resulting in the thickening of the active layer. Consequently, the ice within the pores of the frozen layer melts into water, reducing its volume and leading to ground subsidence. Additionally, the outflow of groundwater from the pores in the active layer reduces the volume of both the active layer and the upper frozen layer, further contributing to subsidence.

3. THE STUDY AREA AND THE SFS

3.1. The Study Area

The study area (64°50′54″ N, 163°42′72″ W) is located in a tundra region approximately 6 km from Council to Nome on the Seward Peninsula of Alaska, USA, at an elevation of around 55 m above the sea level, with a slope to the east (Figure 2). The area comprises unconsolidated sediments deposited since the end of the Cenozoic (Tertiary) Era, while the surrounding mountains contain metamorphic rock complexes, including schist and marble, dating from the Neoproterozoic to the Devonian periods [47].

Climate data were collected from 1980 to 2016 at White Mountain Airport (64°41′07″ N, 163°24′39″W), which is located about 23 km southeast of the study area and at an altitude of about 81 m. The collected data indicate that the lowest mean temperature is −14°C in January, while the highest mean temperature is 13°C in July. The average monthly snowfall begins at 5.5 cm in October and peaks at approximately 18.2 cm in December. The shortest day lasts about 4 hours, whereas the longest day extends to 21 hours and 40 minutes.

In 2015, an automatic weather station was installed in the study area to measure air temperature, along with a wind direction and wind speed recorder positioned at a height of 3 m above the ground. Figure 3(a) illustrates the wind rose diagrams for the winters of 2015 and 2016, indicating that northwesterly winds prevailed during both winters. Figure 3(b) presents a graph of the air temperature from October 2016 to October 2018, and

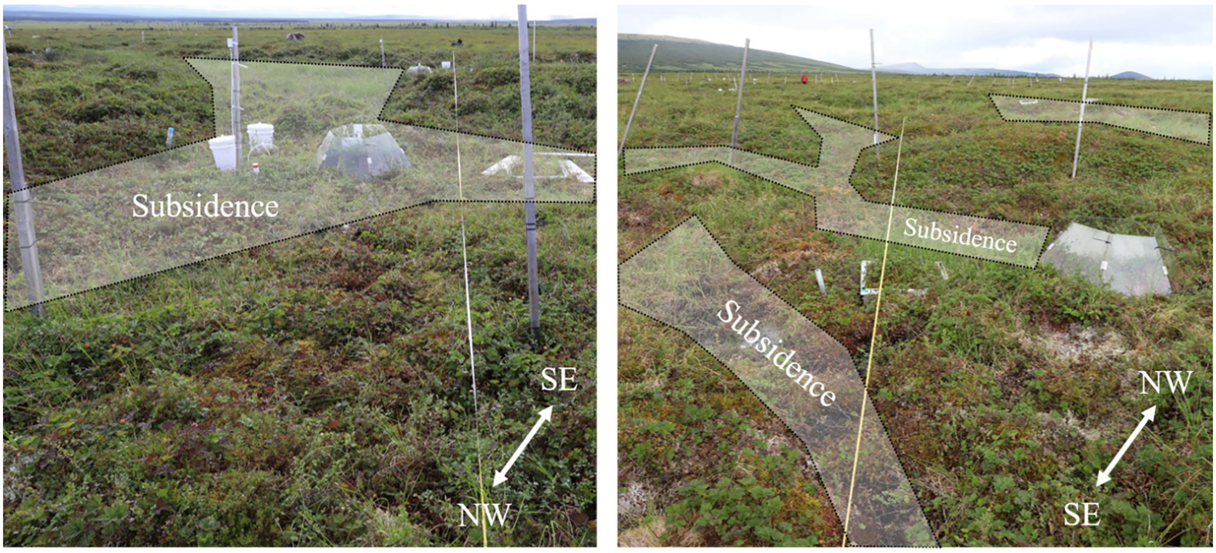

Figure 7: The in situ photograph with ground subsidence marked by white shading. The shooting direction for the left figure is from NW to SE, and the right figure is in the opposite direction.

the average temperature during the period was −1.6°C. Throughout this period, the lowest recorded temperature was −36°C, while the highest reached 22°C, resulting in an annual temperature difference of up to 58°C. Winter temperatures approached 0°C on several occasions, and summer temperatures fluctuated between 10°C and 20°C. The freezing season began at the end of September, while the thawing season began at the end of May.

3.2. SFs

To induce changes in snowfall during winter, SFs are installed perpendicular to the dominant wind direction. When a snowstorm reaches the SF, the speed of the storm slows down due to the resistance of the fence, and the snow transported by the storm accumulates beyond the fence. After that, the amount of snow that accumulates decreases as it moves farther away from the SF. The area around the SF is divided into three zones based on snow cover: the control zone (CZ), where the snowstorm remains unaffected by the SF; the low zone (LZ), where the snow cover is reduced by the SF; and the high zone (HZ), where the snowstorm leads to greater snow accumulation due to the SF (Figure 4).

In particular, according to Kim et al. [48], the HZ is developed in the direction of the wind blowing from the SF and has two distinct characteristics compared to the other zones [48]. ① In this region, snow accumulates earlier than in the other regions, and the accumulated snow acts as insulation. As a result, the snow melts later than in the other regions and the time when the ground is exposed is delayed. ② The ground temperature is higher here because of the large amount of snow accumulated during the winter, and during the thaw period, the snow melts later in this zone than in the other zones, resulting in the ground temperature remaining above 0.0°C for longer than in the other zones.

The density of the snow varies from 100 to 500 kg $\cdot\, m^{-3}$, influenced by the depositional conditions. Fresh snow exhibits a lower density due to the numerous pores between snow particles, whereas compacted snow displays a higher density because these pores are diminished. The pores within snow are air filled, which affects thermal conductivity. At 0.0°C, ice has a thermal conductivity of 2.2 W $\cdot\, m^{-1}K^{-1}$. At 10.0°C, air has a thermal conductivity of 0.025 W $\cdot\, m^{-1}K^{-1}$, and water has a thermal conductivity of 0.57 W $\cdot\, m^{-1}K^{-1}$, making the thermal conductivity of water approximately 22 times greater than that of air [49]. This indicates that the thermal conductivity of snow is relatively low, ranging from 0.08 to 0.42 W $\cdot\, m^{-1}K^{-1}$, depending on the crystallization state of the snow. This low conductivity inhibits the transfer of cold air from the atmosphere to the ground during winter. During the thawing season, as the snow on the ground melts, the pores of the snow become filled with snowmelt water, increasing the thermal conductivity of the snow. Additionally, much of the winter snow cover melts during the thawing season, hydrating the ground and promoting increased vegetation activity. Once the snow cover reaches the height of the SF, the effect of the SF diminishes, and snow accumulation in the CZ and LZ gradually increases due to the significant amount of snow already accumulated in the HZ.

4. THE DATA

To assess how the frozen ground was affected by the SFs installed in 2017, several surveys were conducted. The height of the snow cover and subsurface temperatures around the SFs were observed, and changes in surface topography were recorded through field surveys. To quantitatively identify changes in the terrain of the research area, LiDAR surveys were conducted using a UAV

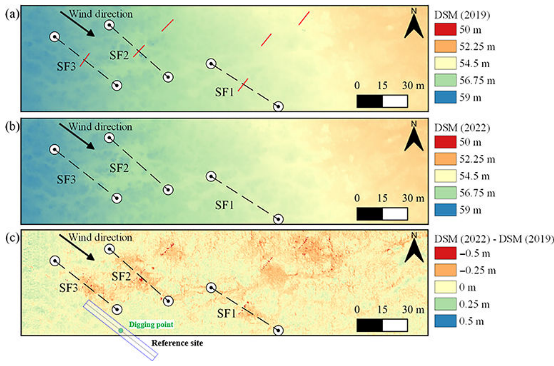

Figure 8: Results of the DSM measurement in (a) 2019, (b) 2022, and (c) their differences. The black arrows indicate the main wind direction in winter, and the red solid and black dashed lines represent the snow fences and geophysical survey lines, respectively.

4.1. SF Data

In this study, SFs measuring 1.2 m in height and 10.0 m in length and featuring multiple 8-cm diameter holes were installed for the first time in September 2017 (Figure 5(a)). The SFs were positioned in a northeast–southwest direction, perpendicular to the prevailing wind, based on the wind data collected in the field. To account for the spatial variability of the area, six SFs were installed. To assess the snow distribution across the SFs, three fences were selected in February 2021, and the snow thickness was measured at 0.1-m intervals, with the results averaged (Figure 5(b)). The measurement lines extended approximately 20.0 m to the left and right of the SF.

The average height of snow cover around the SF varied by zone, with approximately 0.8 m in CZ, 0.9 m in HZ, and 0.6 m in LZ. Notably, around the SF, the ground surface became uneven and bumpy due to localized subsidence compared to areas without the fence. Additionally, puddles formed at various locations, resulting in some areas being relatively wet, which also affected the vegetation. The study area is moist tussock tundra, primarily composed of *Sphagnum* moss, cotton grass (*Eriophorum vaginatum*), blueberry (*Vaccinium uliginosum*), cloudberry (*Rubus chamaemorus*), and labrado tea (*Ledum palustre*) as the main vegetation.

To monitor ground temperature changes in response to variations in air temperature, a series of observations were conducted in each zone at depths to 1.1 m. The

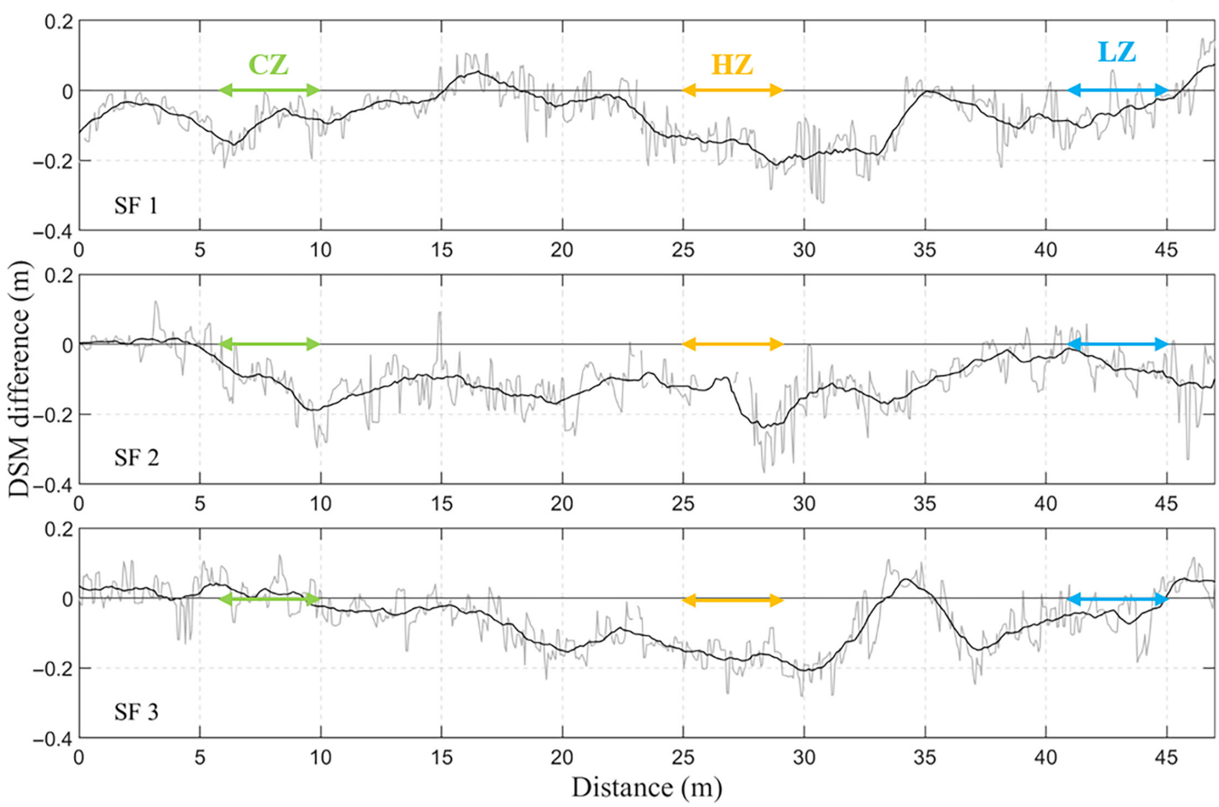

Figure 9: The DSM difference of survey lines for SF 1, SF 2, and SF 3 described in Figure 7(c).

drone in 2019 and 2022. In addition, since changes in the topography of the study area are closely related to changes in the characteristics of the subsurface, geophysical surveys such as ERT and GPR were conducted to obtain subsurface information in the summer of 2023. The main purpose of these geophysical surveys was to identify changes in the lower boundary of the active layer. Both the ERT and GPR surveys covered a total length of approximately 45 m in a northwest–southeast direction, perpendicular to the installed SFs.

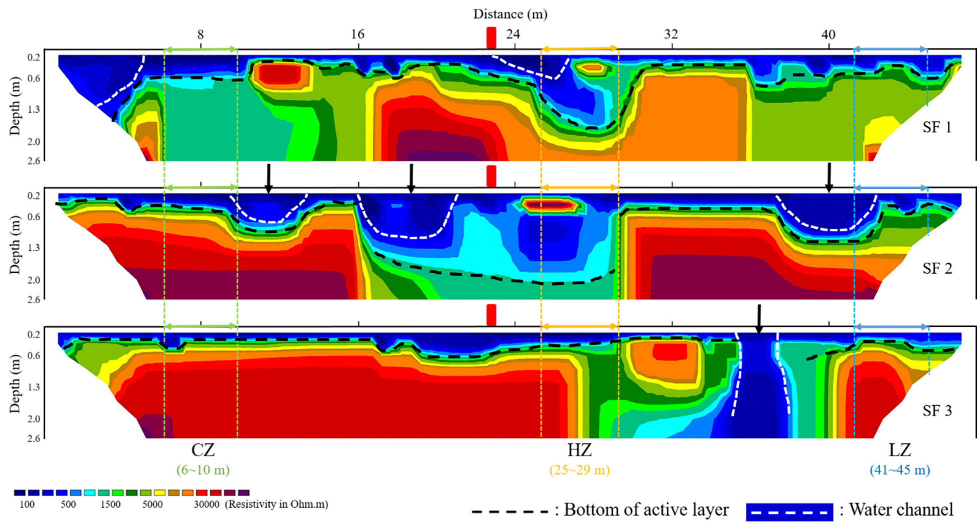

FIGURE 10: Electrical resistivity cross sections obtained from each survey line in Figure 7: (top) SF 1, (middle) SF 2, and (bottom) SF 3. The red tick indicates the position of the SFs at 23 m. The black and white dashed lines represent the bottom of the active layer and the water channel, respectively.

measurement intervals were 0.05 and 0.1 m for depth ranges 0.0–0.3 m and 0.4–1.1 m, respectively [50]. The results are presented in Figures 6(a) through 6(c), showing temperature variations with depth by date for each zone. Figure 6(d) shows a graphical comparison of the temperature changes at a depth of 0.3 m for each zone. The figures include results from October 2019 to October 2020, representing a 1-year period but only up to a depth of 0.6 m, because temperature changes were not significant at relatively greater depths. HZ results were recorded until early June 2020, after which data collection was halted due to equipment issues. Initially, as the freezing season began, the ground temperature fell below 0°C only at the surface. Over time, however, it was observed that the temperature also dropped below 0°C at greater depths. In the LZ, where the least amount of snow accumulated, the temperature dropped to a lower level than in the other zones. Conversely, the temperature in the CZ was higher than in the LZ. This indicates that the influence of atmospheric temperature was less in the CZ, likely due to the differences in snow cover between the two zones. During the same period, in the HZs with the highest snow accumulation, the durations when the ground temperature fell below 0.0°C was relatively short, and the affected depths were minimal. This indicates that the insulating properties of the thick snow layer inhibited the transfer of air temperature to the ground. During the thawing season, the changes in the ground temperatures in the LZ and CZ indicate that the CZ was less sensitive to atmospheric temperature. This underscores the significant influence of the accumulated snow during this period. Figure 6(d) illustrates the ground temperature variation at a depth of 0.3 m across the three zones, revealing the zero-curtain effect at all three sites during the initial stages of freezing and thawing. This phenomenon is attributed to phase changes in moisture, which absorb and release latent heat, to maintain a temperature of 0.0°C [51]. During the winter, a significant temperature difference was observed across the three zones. The lowest temperature recorded in HZ was approximately −1.0°C, while in CZ it reached around −3.8°C, and in LZ it dropped to approximately −4.8°C. A notable temperature difference was observed between the HZ and the other two zones. Although data for the HZ are unavailable, the temperature contrast between LZ and CZ during the thawing season remains clear.

Figure 7 is a photograph taken in July 2023 showing subsidence at the actual site, with wooden poles indicating the locations of the SFs. Several areas can be seen where the terrain is lower than the surrounding area. After the initial installation of six SFs in the study area in the fall 2017, most of the research equipment and structures that had been leveled began to tilt during the annual process of equipment installation and dismantling. Although they were releveled and reinstalled, they tilted again in the following year. In contrast to the first year after installing the SFs, water began to pool in certain areas, forming puddles and waterways based on elevation differences. The melting of accumulated winter snow led to the pooling of water in the study area, resulting in the creation of water channels, as confirmed through visual inspection. These topographic changes were only observed around the SF and not in areas away from it near the study area. Therefore, they are considered to be the effect of the SF rather than a result of soil or vegetation changes.

4.2. Remote Sensing Data

LiDAR is a remote sensing technology that uses laser light to measure distances by illuminating targets and analyzing reflected signals. This technology is favored for its high accuracy, efficiency, and cost-effectiveness in various remote sensing applications. Field measurements in the study area were conducted on September 26, 2019, and August 18, 2022. These measurements involved acquiring point clouds, which are a collection of points defined by

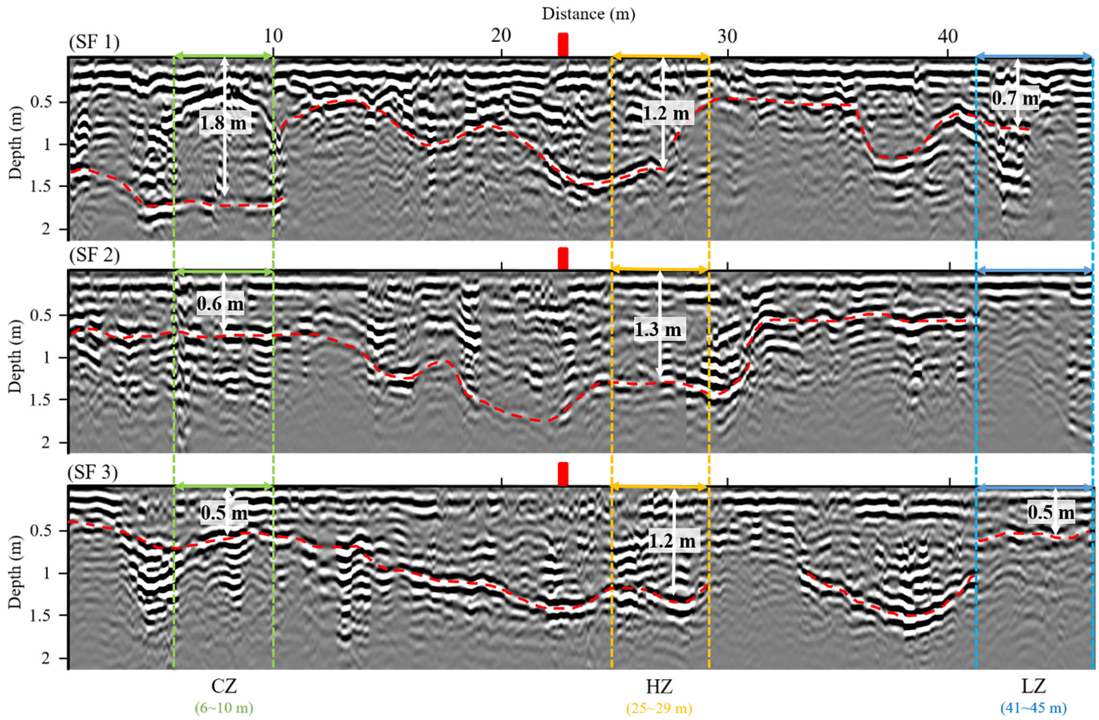

Figure 11: The GPR cross sections obtained from each of the survey lines depicted in Figure 8: (top) SF 1, (middle) SF 2, and (bottom) SF 3. The red dashed lines indicate the bottom boundaries of the active layer. The red tick lines indicate the SF position at 23 m.

precise *X*, *Y*, and *Z* coordinates. A compact LiDAR sensor, Velodyne Puck Hi-Res (Velodyne Acoustics, Hamburg, Germany), was used for this purpose (refer to the datasheet in Table 1). This sensor was integrated with a survey-grade global navigation satellite system/IMU, specifically the Trimble APX-15 (Trimble Applanix, Ontario, Canada), and was mounted on a DJI Matrice 600 Pro drone (DJI, Shenzhen, China). The practical vertical accuracy of this sensor system is approximately 1–2 cm, as demonstrated in previous studies [52]. The LiDAR points were subsequently processed to accurately represent the Earth's surface through the generation of a digital surface model (DSM). This process includes several key steps: (1) noise filtering to eliminate erroneous points caused by atmospheric interference or reflective surfaces; (2) classification to distinguish between ground points, vegetation, and other structures; and (3) interpolation to form a continuous surface from discrete LiDAR point clouds using established interpolation techniques [53]. Ultimately, DSMs with a spatial resolution of 10 cm were generated from the LiDAR point clouds, as depicted in Figures 8(a) and 8(b).

The results of the remote sensing analysis reveal that the study area has a west-to-east slope with an elevation of approximately 55 m around the SF. Figure 8(a) shows the location of the SFs marked by red solid lines. The dark blue dots around the fence indicate higher altitude, representing the locations of facilities installed for research related to the SFs. Figure 8(b) shows the DSM obtained in August 2022, after removing all facilities. Figure 8(c) illustrates the changes in the DSM over a 3-year period by comparing the 2022 data with the 2019 data; a negative value indicates ground subsidence. In the figure, the elevation at the SF installation points has decreased due to the removal of the fence itself. Additionally, ground subsidence has been observed around these points. Notably, the ground subsidence area is more pronounced in the southeastern region than in the northwestern region relative to the SF. To enable a comparative analysis of the DSM changes, three representative SFs, shown in Figure 9, were selected from the original six SFs. In Figure 9, the survey line begins at the northwest point (0 m) and ends at the southeast (47 m) point with the SF positioned approximately 23 m along the survey line. The graphs indicate ground subsidence along most of the survey line. Notably, the most significant subsidence occurred within the 25–30 m zone of the HZ, with an average depth of approximately 0.2 m and a maximum of approximately 0.35 m. The CZs of SF 1 and SF 2 exhibit subsidence, as shown in Figures 9(a) and 9(b), whereas the CZ of SF 3 exhibits no subsidence (Figure 9(c)). The positive values observed in the graphs are due to vegetation changes.

4.3. Electrical Resistivity Data

This study used the Wenner electrode configuration for electrical resistivity investigations, which is ideal for shallow horizontal surveys and exhibits high sensitivity to horizontal inhomogeneities [54]. Here, the electrode spacing was set to 1 m with 48 electrodes employed. The inverted 2D cross sections of the subsurface were obtained using Res2DINV software, which is widely used in data processing to generate an electrical resistivity cross section of the subsurface. The electrical resistivity characteristics of the subsurface, as determined by data processing, vary

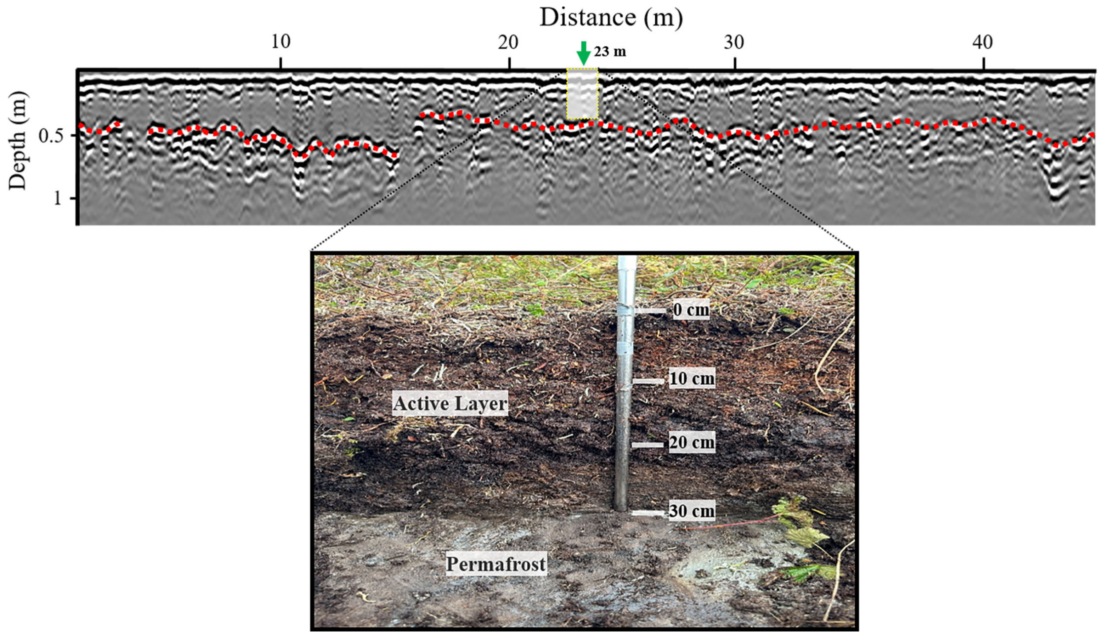

Figure 12: The GPR cross section and digging results obtained at the digging point presented in Figure 2. The snow fence did not hinder the site.

according to the environmental conditions. It is well-known that frozen soil such as permafrost typically has an electrical resistivity above $1000\Omega \cdot m$, clay usually falls below $100\Omega \cdot m$, and the electrical resistivity of alluvial soils varies depending on their sand content [55]. These reference values are valuable resources for interpreting the survey results.

Figure 10 presents the inverted 2D subsurface model for SF 1, SF 2, and SF 3. SF 1, located at the lowest elevation of the three SFs, was likely affected by snowmelt water flowing in from the relatively higher elevations of SF 2 and SF 3, leading to the formation of a broad, low electrical resistivity zone. Along the survey line, from 0 m to about 10 m, the thickness of the active layer was estimated to be around 1 m, which corresponds well with the water channel observed in the drone image in Figure 2. Notably, the active layer is thicker in the HZ, which is attributed to the thawing of the upper layer of the permafrost. Beyond 32 m in the survey line, the thickness of the active layer becomes inconsistent, which is attributed to soil inhomogeneity and topographic influences.

In the SF 2 data, the active layer measured about 0.5 m thick, ranging from 0 m to approximately 15 m along the survey line, indicating that the snow cover did not have a significant impact on the active layer. However, the electrical resistivity values showed substantial variation up to 8 m on either side of the SF, where the thickness of the active layer with low electrical resistivity values ranged from approximately 1.5 m to 2 m. This was the thickest zone identified in SF 2 and is likely due to the high accumulation of snow by the SF, which resulted in more thawing of the upper part of the permafrost compared to other areas. Near the 40-m mark of the survey line, where the active layer exceeded 1.0 m in thickness, snowmelt water from the SF 3 region was continuously accumulating, forming a water channel in the area and resulting in low electrical resistivity values.

In SF 3, which had the highest elevation values, the active layer measured less than 0.5 m thick, ranging from 0 m to 18 m along the survey line, and appeared to be unaffected by snow cover. Notably, unlike SF 1, this section was not influenced by the SF. The active layer began to thicken at the 18 m mark along the survey line, and by 35 m, snowmelt water had accumulated, forming a water channel. This accumulation caused the upper part of the permafrost to thaw, resulting in the active layer reaching a thickness of more than 2 m. The active layer thickness varied significantly across the three SF sites.

4.4. GPR Data

A GPR survey is a technique that uses high-frequency EM wave signals reflected from the subsurface to gather data. In a GPR survey, resolution refers to the ability to distinguish between two adjacent, reflected signals at the receiver and is proportional to the frequency of the source. This is because the frequency and speed of the EM wave in the medium determine the wavelength. For the thawed and frozen layers in an environment such as the study area, the EM wave speeds are approximately 0.06 m/ns and 0.106 to 0.202 m/ns, respectively [56]. Consequently, for a 250 MHz antenna, the wavelengths in the thawed and frozen layers would be 0.24 m and 0.424–0.808 m, respectively, resulting in theoretical vertical resolutions of 0.06 m and 0.106 to 0.202 m. Using a 500 MHz antenna, the vertical resolution would improve to 0.03 m or 0.053–0.101 m, respectively.

In this study, the GPR survey employed EM waves with a center frequency of 250 MHz as the transmitting source.

GPR data were collected at 0.1-m intervals using step mode, with a distance of 0.36 m maintained between the transmitter and receiver antennas to ensure data reliability. Additionally, GPR data were gathered using a 500 MHz center frequency antenna in a clean area near the SFs, where the influence of the SF was absent. This approach allowed for an intuitive comparison of the changes in the thickness of the active layer relative to the data collected around the SF.

Figure 11 presents the results of the GPR survey performed on the three SFs. For SF 1, the active layer from 0.0 m to 10.0 m along the survey line was approximately 1.5 m deep, consistent with the findings from the electrical resistivity survey. From 15.0 m to 30.0 m along the survey line, the active layer thickened, reaching a maximum depth of 1.5 m. Between 30.0 m and 35.0 m, the active layer was approximately 0.5 m, with varying thicknesses between 0.5 m and 1.0 m in the remaining zones. In the SF 2 area, the active layer from 0.0 m to 15.0 m along the survey line was about 0.6 m thick and increased to 1.0 m to 1.5 m around the SF. Beyond 30 m, the thickness of the active layer thinned to 0.5 m, with a notably weak signal from 41.0 m to 44.0 m along the survey line, suggesting strong signal attenuation due to significant water presence in the water channel. SF 3, positioned at the highest elevation, displayed an active layer thickness of approximately 0.5 m, ranging from 0.0 m to 10.0 m along the survey line. The thickness steadily increased until the HZ (24.0 m to 29.0 m along the survey line), where it reached a maximum of approximately 1.5 m. The GPR data from all three fences indicated that the thickness of the active layer varied in the LZ, CZ, and HZ. Notably, the approximate thickness of the active layer in the HZ was around 1.5 m, which is more than twice the depth of the active layer in the LZ.

The GPR survey results along the survey lines of SF 1 to SF 3 confirmed that the thickness of the active layer increases with increasing snow cover. To intuitively verify these features, a reference site was selected away from the SF, where the snow cover was not influenced by the fence. A GPR survey was conducted there to assess the subsurface characteristics of the study area without the influence of the SF.

Figure 12 shows the result of the GPR survey conducted using a 500 MHz antenna, which illustrates the thickness of the active layer in the absence of any SF influence. The results indicate that the active layer was 0.3 m to 0.5 m thick, and the actual excavation revealed that the active layer reached a depth of 0.3 m, with an ice-rich permafrost layer identified beneath it. Therefore, it can be concluded that, in the absence of changes to snow cover, the active layer in the study area was up to 0.5 m thick. This result was compared to the maximum active layer thickness of 2.0 m in the HZ, where snow cover was increased by the SF. Hence, this finding confirmed that the change in snow cover caused by the SF had increased the thickness of the active layer and was responsible for the observed ground subsidence.

5. CONCLUSION

In this study, SFs were installed in 2017 in a northeast–southwest orientation, perpendicular to the prevailing winter wind direction in the area, to induce changes in snow cover and analyze their impact on the in Alaska tundra. The results of a field survey conducted in February 2021 confirmed that ground subsidence had occurred around the SFs. Various geophysical surveys were then carried out to examine the relationship between the ground subsidence and the SFs.

Remote sensing, conducted using an UAV drone equipped with a LiDAR sensor, provided high-accuracy DSM to quantify ground subsidence. The DSM data acquired in 2019 and 2022 confirmed that approximately 0.2 m of ground subsidence occurred around the SFs, with the most significant subsidence concentrated in the HZ, where snow cover increased markedly. To further investigate the relationship between the SF and ground subsidence, ERT and GPR surveys were conducted to analyze the subsurface conditions. These two geophysical methods effectively delineated the boundary between the active layer and permafrost, clearly identifying the change in the thickness of the active layer caused by the SF.

The causes of ground subsidence identified through various investigations in this study are as follows. The SF increased snow cover, particularly in the HZ, which enhanced the insulating effect and delayed the influence of low winter temperatures on the subsurface. This delay caused the subsurface temperature to remain above 0°C for a longer period, increasing the thickness of the active layer by melting the top of the permafrost. Additionally, GPR survey results from areas unaffected by the SF support the finding that increased snow cover thickens the active layer. The thickening of the active layer triggered the melting of frozen water in the voids, which, combined with runoff and compaction, led to subsidence. Furthermore, the outflowing pore water formed channels that flowed eastward across the SF, as observed in the DSM images and geophysical survey data. These results clearly demonstrate that changes in snow cover can influence the active layer, leading to localized environmental changes and ground subsidence.

Data Availability

The data of this study are available in the manuscript. Requests to access the datasets can be directed to the corresponding authors Joohan Lee and Won-Ki Kim.

Conflicts of Interest

The authors declare that they have no conflicts of interest.

Funding Statement

This research was supported by Korea Institute of Marine Science & Technology Promotion (KIMST) grant funded by the Ministry of Oceans and Fisheries (KIMST

RS-2021-KS211509), a National Research Foundation of Korea Grant from the Korean Government (MSIT ; the Ministry of Science and ICT) (NRF-2021M1A5A1075508) (KOPRI-PN24012), and Korea Institute of Marine Science & Technology Promotion (KIMST) funded by the Ministry of Oceans and Fisheries, Korea (RS-2023-00259633). Additional support was provided by Baptiste Dafflon under the Next Generation Ecosystem Experiment (NGEE) Arctic project funded by the U.S. Department of Energy, Office of Biological and Environmental Research under contact DEAC02-05CH11231.

Acknowledgments

We thank Patrick McClure, Stijn Wielandt, Chen Wang, Ian Shirley, and Jack Lamb for assistance with soil temperature instrumentation.

References

[1] X. Wang, T. Wang, H. Guo, et al., "Disentangling the mechanisms behind winter snow impact on vegetation activity in Northern ecosystems", *Global Change Biology*, vol. 24, no. 4, pp. 1651–1662, 2018.

[2] M. R. McCrystall, J. Stroeve, M. Serreze, B. C. Forbes, and J. A. Screen, "New climate models reveal faster and larger increases in Arctic precipitation than previously projected", *Nature Communications*, vol. 12, no. 1, 2021.

[3] F. M. Nixon and A. E. Taylor, "Regional active layer monitoring across the sporadic, discontinuous and continuous permafrost zones, Mackenzie valley, Northwestern Canada", in *In Proceeding of the 7thInternational Permafrost Conference*, 55:pp. 815–820, 1998.

[4] J. Brown, K. M. Hinkel, and F. E. Nelson, "The circumpolar active layer monitoring (calm) program: Research designs and initial results", *Polar Geography*, vol. 24, no. 3, pp. 166–258, 2000.

[5] M. J. Lafrenière, E. Laurin, and S. F. Lamoureux, "The impact of snow accumulation on the active layer thermal regime in high arctic soils", *Vadose Zone Journal*, vol. 12, no. 1, pp. 1–13, 2013.

[6] K. M. Hinkel and J. K. Hurd Jr, "Permafrost destabilization and thermokarst following snow fence installation, Barrow, Alaska, U.S.A.", *Arctic, Antarctic, and Alpine Research*, vol. 38, no. 4, pp. 530–539, 2006.

[7] T. E. Osterkamp, R. W. Jurick, G. A. Gislason, and S.-I. Akasofu, "Electrical resistivity measurements in permafrost terrain at the engineer creek road cut, fairbanks, Alaska", *Cold Regions Science and Technology*, vol. 3, no. 4, pp. 277–286, 1980.

[8] S. Wipf and C. Rixen, "A review of snow manipulation experiments in arctic and alpine Tundra ecosystems", *Polar Research*, vol. 29, no. 1, pp. 95–109, 2010.

[9] H. B. O'Neill and C. R. Burn, "Impacts of variations in snow cover on permafrost stability, including simulated snow management, dempster highway, peel plateau, Northwest territories", *Arctic Science*, vol. 3, no. 2, pp. 150–178, 2017.

[10] Y. J. Kim, J. Hyun, A. Michelsen, E. E. Kwon, and J. Y. Jung, "Key determinants of soil labile nitrogen changes under climate change in the arctic: A meta-analysis of the responses of soil labile nitrogen pools to experimental warming and snow addition", *Chemical Engineering Journal*, vol. 494, p. 153066, 2024.

[11] T. H. Maiman, "Stimulated optical radiation in ruby", *Nature*, vol. 187, no. 4736, pp. 493–494, 1960.

[12] C. T. Ackerman, Linking geographic information systems(GIS) with hydraulic modeling using ARC/INFO and HEC-RAS, University of California, 1999.

[13] A. Bhardwaj, L. Sam, A. Bhardwaj, and F. J. Martín-Torres, "LiDAR remote sensing of the cryosphere: Present applications and future prospects", *Remote Sensing of Environment*, vol. 177, pp. 125–143, 2016.

[14] A. Suprem, V. Deep, and T. Elarabi, "Orientation and displacement detection for smartphone device based imus", *IEEE Access*, vol. 5, pp. 987–997, 2017.

[15] L. Wallace, A. Lucieer, C. Watson, and D. Turner, "Development of a UAV-lidar system with application to forest inventory", *Remote Sensing*, vol. 4, no. 6, pp. 1519–1543, 2012.

[16] J. M. Reynolds, "Electrical resistivity of george VI ice shelf, Antarctic Peninsula", *Annals of Glaciology*, vol. 3, pp. 279–283, 1982.

[17] J. M. Reynolds and J. G. Paren, "Electrical resistivity of ice from the Antarctic Peninsula, Antarctica", *Journal of Glaciology*, vol. 30, no. 106, pp. 289–295, 1984.

[18] R. D. Barker, "A simple algorithm for electrical imaging of the subsurface", *First Break*, vol. 10, no. 2, pp. 53–62, 1992.

[19] J. M. Reynolds and D. M. McCann, "Geophysical methods foe assessment of landfill and waste disposal sites", in *in Proceedings of 2nd International Conference on Polluted and Marginal Land*, pp. 63–71, Engineering Technics Press, Edinburgh, 1992.

[20] B. Rana, A. B. Shrestha, J. M. Reynolds, R. Aryal, A. P. Pokhrel, and K. P. Budhathoki, "Hazard assessment of the tsho roipa glacier lake and ongoing remediation measures", *Journal of Nepal Geological Society*, vol. 22, pp. 563–570, 2000.

[21] H.-S. Kwon, Y. Song, M.-J. Yi, H.-J. Chung, and K.-S. Kim, "Case histories of electrical resistivity and controlled-source magnetotelluric surveys for the site investigation of tunnel construction", *Journal of Environmental and Engineering Geophysics*, vol. 11, no. 4, pp. 237–248, 2006.

[22] E. D. Trochim, W. E. Schnabel, M. Kanevskiy, J. Munk, and Y. Shur, "Geophysical and cryostratigraphic investigations for road design in Northern Alaska", *Cold Regions Science and Technology*, vol. 131, pp. 24–38, 2016.

[23] C. H. Conaway, C. D. Johnson, T. D. Lorenson, et al., "Permafrost mapping with electrical resistivity tomography: A case study in two wetland systems in interior Alaska", *Journal of Environmental and Engineering Geophysics*, vol. 25, no. 2, pp. 199–209, 2020.

[24] M. Rossi, M. Dal Cin, S. Picotti, et al., "Active layer and permafrost investigations using geophysical and geocryological methods—A case study of the Khanovey area, near Vorkuta, in the NE European Russian Arctic", *Frontiers in Earth Science*, vol. 10, 2022.

[25] A. Tourei, X. Ji, G. Rocha dos Santos, et al., "Mapping permafrost variability and degradation using seismic surface waves, electrical resistivity, and temperature sensing: A case

study in Arctic Alaska”, *Journal of Geophysical Research*, vol. 129, no. 3, 2024.

[26] X. Zeng and G. A. McMechan, “GPR characterization of buried tanks and pipes”, *GEOPHYSICS*, vol. 62, no. 3, pp. 797–806, 1997.

[27] S. A. Arcone, E. F. Chacho, and A. J. Delaney, “Seasonal structure of taliks beneath Arctic streams determined with ground-penetrating radar”, *Permafrost*, 55, 1998.

[28] S. P. Carter, D. D. Blankenship, M. E. Peters, D. A. Young, J. W. Holt, and D. L. Morse, “Radar-based subglacial lake classification in Antarctica”, *Geochemistry, Geophysics, Geosystems*, vol. 8, no. 3, p. 3, 2007.

[29] C. Hauck and C. Kneisel, 240p, Applied geophysics in periglacial environments, Cambridge University Press, 2009.

[30] Y. You, Q. Yu, X. Pan, X. Wang, and L. Guo, “Geophysical imaging of permafrost and talik configuration beneath a thermokarst lake”, *Permafrost and Periglacial Processes*, vol. 28, no. 2, pp. 470–476, 2017.

[31] L. E. Lindzey, L. H. Beem, D. A. Young, et al., “Aerogeophysical characterization of an active subglacial lake system in the david glacier catchment, Antarctica”, *The Cryosphere*, vol. 14, no. 7, pp. 2217–2233, 2020.

[32] A. Rutishauser, D. D. Blankenship, D. A. Young, et al., “Radar sounding survey over devon ice cap indicates the potential for a diverse hypersaline subglacial hydrological environment”, *The Cryosphere*, vol. 16, no. 2, pp. 379–395, 2022.

[33] E. Richards, S. Stuefer, R. C. Rangel, C. Maio, N. Belz, and R. Daanen, “An evaluation of GPR monitoring methods on varying river ice conditions: A case study in Alaska”, *Cold Regions Science and Technology*, vol. 210, p. 103819, 2023.

[34] B. J. Minsley, J. D. Abraham, B. D. Smith, et al., “Airborne electromagnetic imaging of discontinuous permafrost”, *Geophysical Research Letters*, vol. 39, no. 2, 2012.

[35] M. A. Briggs, S. Campbell, J. Nolan, et al, “Surface geophysical methods for characterising frozen ground in transitional permafrost landscapes”, *Permafrost and Periglacial Processes*, vol. 28, no. 1, pp. 52–65, 2017.

[36] I. Buddo, M. Sharlov, I. Shelokhov, et al., “Applicability of transient electromagnetic surveys to permafrost imaging in Arctic West Siberia”, *Energies*, vol. 15, no. 5, p. 1816, 2022.

[37] C. Harris and J. D. Cook, “The detection of high altitude permafrost in jotunheimen, Norway using seismic refraction techniques: An assessment”, *Arctic and Alpine Research*, vol. 18, no. 1, pp. 19–26, 1986.

[38] M. Musil, H. Maurer, A. G. Green, et al., “Shallow seismic surveying of an alpine rock glacier”, *GEOPHYSICS*, vol. 67, no. 6, pp. 1701–1710, 2002.

[39] A. Ikeda, “Combination of conventional geophysical methods for sounding the composition of rock glaciers in the Swiss Alps”, *Permafrost and Periglacial Processes*, vol. 17, no. 1, pp. 35–48, 2006.

[40] H. Maurer and C. Hauck, “Geophysical imaging of alpine rock glaciers”, *Journal of Glaciology*, vol. 53, no. 180, pp. 110–120, 2007.

[41] C. Hilbich, “Time-lapse refraction seismic tomography for the detection of ground ice degradation”, *The Cryosphere*, vol. 4, no. 3, pp. 243–259, 2010.

[42] T. Zhang, R. G. Barry, K. Knowles, J. A. Heginbottom, and J. Brown, “Statistics and characteristics of permafrost and ground-ice distribution in the Northern Hemisphere”, *Polar Geography*, vol. 31, nos. 1–2, pp. 47–68, 2008.

[43] M.-K. Woo, Permafrost hydrology, Springer, 2012.

[44] D. L. Kane, L. D. Hinzman, and J. P. Zarling, “Thermal response of the active layer to climatic warming in a permafrost environment”, *Cold Regions Science and Technology*, vol. 19, no. 2, pp. 111–122, 1991.

[45] A. H. Lachenbruch, “Permafrost, the active layer, and changing climate”, *U.S. Geological Survey*, 1994.

[46] O. T. Farouki, “The thermal properties of soils in cold regions”, *Cold Regions Science and Technology*, vol. 5, no. 1, pp. 67–75, 1981.

[47] W. Frederic H., H. Chad,Mull Charles G., and K. Susan M, “Geologic map of alaska”, *Scientific Investigations Map 3340*, 2015

[48] K. Kim, J. Lee, H. Ju, et al., “Time-lapse electrical resistivity tomography and ground penetrating radar mapping of the active layer of permafrost across a snow fence in Cambridge bay, Nunavut territory, Canada: Correlation interpretation using vegetation and meteorological data”, *Geosciences Journal*, vol. 25, no. 6, pp. 877–890, 2021.

[49] T. R. Oke, *Boundary Layer Climates*. 2nd edition, Routledge, London, 1987.

[50] B. Dafflon, S. Wielandt, J. Lamb, et al., “A distributed temperature profiling system for vertically and laterally dense acquisition of soil and snow temperature”, *The Cryosphere*, vol. 16, no. 2, pp. 719–736, 2022.

[51] S. I. Outcalt, F. E. Nelson, and K. M. Hinkel, “The zero-curtain effect: Heat and mass transfer across an isothermal region in freezing soil”, *Water Resources Research*, vol. 26, no. 7, pp. 1509–1516, 1990.

[52] J. Chi, J.-I. Kim, S. Lee, et al., “Geometric and radiometric quality assessments of UAV-borne multi-sensor systems: Can uavs replace terrestrial surveys?”, *Drones*, vol. 7, no. 7, p. 411, 2023.

[53] J. Kim, J. Chi, A. Masjedi, et al, “High-resolution hyperspectral imagery from pushbroom scanners on unmanned aerial systems”, *Geoscience Data Journal*, vol. 9, no. 2, pp. 221–234, 2022.

[54] A. Samouëlian, I. Cousin, A. Tabbagh, A. Bruand, and G. Richard, “Electrical resistivity survey in soil science: A review”, *Soil and Tillage Research*, vol. 83, no. 2, pp. 173–193, 2005.

[55] J. M. Reynolds, “The role of surface geophysics in the assessment of regional groundwaterpotential in Northern Nigeria”, *Geological Society, London, Engineering Geology Special Publications*, vol. 4, no. 1, pp. 185–190, 1987.

[56] J. M. Reynolds, “An introduction to applied and environmental geophysics.”, 2nd edition, Wiley–blackwell, 2011.

[57] K. Kim, E. Lee, H. Ju, J. Lee, and W.-K. Kim, “Changes in vegetation distribution around the king sejong station in antarctica: A comprehensive analysis of time-lapse electrical resistivity data, meteorological data, and vegetation data”, *Lithosphere*, vol. 2024, no. 4, p. 4, 2024.